Front. Mech. Eng. 2023, 18(1): 4
https://doi.org/10.1007/s11465-022-0720-4

RESEARCH ARTICLE

Mechanical behavior and semiempirical force model of aerospace aluminum alloy milling using nano biological lubricant

Zhenjing DUAN[a,b], Changhe LI (✉)[a], Yanbin ZHANG (✉)[c], Min YANG[a], Teng GAO[a], Xin LIU[b], Runze LI[d], Zafar SAID[e], Sujan DEBNATH[f], Shubham SHARMA[g]

[a] *School of Mechanical and Automotive Engineering, Qingdao University of Technology, Qingdao 266520, China*
[b] *School of Mechanical Engineering, Dalian University of Technology, Dalian 116024, China*
[c] *State Key Laboratory of Ultra-precision Machining Technology, Department of Industrial and Systems Engineering, The Hong Kong Polytechnic University, Hong Kong 999077, China*
[d] *Department of Biomedical Engineering, University of Southern California, Los Angeles, CA 90089-1111, USA*
[e] *College of Engineering, University of Sharjah, Sharjah 27272, United Arab Emirates*
[f] *Mechanical Engineering Department, Curtin University, Miri 98009, Malaysia*
[g] *Department of Mechanical Engineering, IK Gujral Punjab Technical University, Punjab 144603, India*

✉ *Corresponding author. E-mails: sy_lichanghe@163.com (Changhe LI); zhangyanbin1_qdlg@163.com (Yanbin ZHANG)*

ABSTRACT Aerospace aluminum alloy is the most used structural material for rockets, aircraft, spacecraft, and space stations. The deterioration of surface integrity of dry machining and the insufficient heat transfer capacity of minimal quantity lubrication have become the bottleneck of lubrication and heat dissipation of aerospace aluminum alloy. However, the excellent thermal conductivity and tribological properties of nanofluids are expected to fill this gap. The traditional milling force models are mainly based on empirical models and finite element simulations, which are insufficient to guide industrial manufacturing. In this study, the milling force of the integral end milling cutter is deduced by force analysis of the milling cutter element and numerical simulation. The instantaneous milling force model of the integral end milling cutter is established under the condition of dry and nanofluid minimal quantity lubrication (NMQL) based on the dual mechanism of the shear effect on the rake face of the milling cutter and the plow cutting effect on the flank surface. A single factor experiment is designed to introduce NMQL and the milling feed factor into the instantaneous milling force coefficient. The average absolute errors in the prediction of milling forces for the NMQL are 13.3%, 2.3%, and 7.6% in the *x*-, *y*-, and *z*-direction, respectively. Compared with the milling forces obtained by dry milling, those by NMQL decrease by 21.4%, 17.7%, and 18.5% in the *x*-, *y*-, and *z*-direction, respectively.

KEYWORDS milling, force, nanofluid minimum quantity lubrication, aerospace aluminum alloy, nano biological lubricant

1 Introduction

Aerospace aluminum alloy is the most used structural material for rockets, aircraft, spacecraft, and space stations. These components can be used in complex environments, especially in coastal areas, where corrosive air can affect aircraft structures. Wahab et al. [1] demonstrated that the internal environment of the aircraft, the cargo loaded in the cargo hold, and the misoperation of the aircraft can adversely affect the load-bearing structural components of the aircraft. The force of structural parts is complex. Oguri [2] found that the structural parts of aircraft will be subjected to large loads and easily form structural damage during the process of takeoff, flight, and landing. Yang et al. [3] pointed out that various kinds of damage and corrosion of structural parts will accumulate if the load of aircraft structural parts is under long-term and alternating loads. The milling quality of workpieces determines their impact condition, mechanical wear, service life, corrosion, and environmental and chemical degradation under cyclic load [4–6].

Received March 13, 2022; accepted June 29, 2022

The milling force plays a crucial part in determining the material removal and surface integrity of the workpiece. The manufacturing accuracy and processing quality of structural parts are guaranteed through the coordinated control of milling parameters, tools, material properties, and others [7–10]. The milling force is also important to the prediction of machine tool vibration, geometric accuracy, and stability [11–13].

Three main ways can be used to establish a milling force model. The empirical model is based on experimental data and uses multiple regression analysis to establish an empirical formula for expressing the mathematical relation between force and parameters. The finite element method inputs the workpiece material properties, tool parameters, milling parameters, and cooling conditions through the simulation platform. It also outputs the milling force through certain numerical calculations. Liao et al. [14] reported that the instantaneous milling force model is composed of milling thickness, micro-unit milling force model, and force coefficients, which can show the variation waveform of milling force with the rotation of the milling cutter. Farhadmanesh and Ahmadi [15] believed that the instantaneous milling force model is a frequently used method to calculate the force in the milling process.

At present, Zheng et al. [16] used the differential discrete method to create the force model. Yun and Cho [17] obtained the instantaneous milling force coefficient from the experimental data and established the force model, while Desai et al. [18] established the instantaneous cutting thickness model by using an implicit algorithm. Montgomery and Altintas [19] considered the friction between the flank of the milling tool and the workpiece and created the instantaneous milling force model. Rao et al. [20] studied the surface geometry of the tool deflection milling due to the milling forces and surface errors.

The process of machining requires not only ensuring the processing quality but also conducting in-depth and detailed research on the milling force. In earlier studies, Koenigsberger and Sabberwal [21] developed the milling force equation using mechanical modeling. Sutherland and DeVor [22] supposed that mechanical methods have been widely used for force prediction, and Budak and Altintas [23] extended these methods to predict the deflection and shape errors of related mechanical components. Armarego and Whitfield [24] used the oblique milling force model and the orthogonal milling database to predict the milling force coefficient, which is suitable for complex milling cutter geometry and multi-axis milling operations. Researchers have studied the mechanical properties of orthogonal and oblique cutting in many works [25,26]. The process mechanics formulas in these studies are similar, but they obviously differ in the methods of realizing the cutting force prediction model in the actual process. The modeling process of cutting force is generally realized by establishing the empirical relationship of cutting force through the cutting force coefficients. The prediction accuracy of the cutting force coefficients affects the prediction accuracy of cutting force to a great extent. Therefore, an effective calibration method of cutting coefficient is the key to cutting force modeling [27–29]. Arnaud et al. [30] simulated the cutting process under dry conditions and obtained the cutting force coefficient according to the cutting force. Zaghbani and Songmene [31] obtained the milling force coefficient of dry high-speed milling of Al6061-T6 and Al7075-T6 and established the instantaneous milling force model. Merdol [32] established and verified the instantaneous milling force model of the sawtooth end milling cutter under dry machining conditions. Gradišek et al. [33] established the semiempirical mechanism identification expression of the milling force coefficient of general spiral end mills under the condition of a small amount of lubrication. Wan et al. [34] established a unified instantaneous milling force model of variable geometry end milling cutter. Sun et al. [35] analyzed the geometry of the cutting layer and obtained the mathematical model of the corresponding cutting force. Cai et al. [36] determined the transient milling force coefficient of slender end milling tool under the action of vibration.

Lubrication condition is also a key factor in establishing the milling force model. The milling cooling lubrication mode of aerospace aluminum alloy mainly consists of flood, dry, and minimal quantity lubrication (MQL). Among them, the flood uses a large amount of cutting fluid, which causes pollution to the environment. The waste liquid of cutting fluid must be treated and discharged after reaching the standard. Coz et al. [37] found that the cost of processing cutting fluid is high, which reaches 54% of the cost of cutting fluid. For dry cutting, friction adhesion and other phenomena will occur at the tool/workpiece interface due to the lack of lubrication in the cutting area, and these conditions will deteriorate the surface quality of the workpiece. The chips also accumulate on the material surface due to the inability to remove them, and a large amount of heat is transferred to the tool and workpiece; this condition ultimately results in the secondary hardening of the workpiece under high temperature and pressure, the serious burn of the workpiece surface, and aggravation of tool wear [38,39]. MQL is a green, efficient, and scientific cooling lubrication method, which vaporizes compressed air with a very small amount of lubricant to form a mist in the millimeter and micron levels; this mist is sprayed into the cutting zone to cool and lubricate the tool/workpiece and tool/chip contact interfaces [40,41]. Nanofluid minimal quantity lubrication (NMQL) is a nanofluid prepared by adding nanoparticles to micro lubricating base oil, adding an appropriate amount of dispersant, and mixing by ultrasonic vibration; it is

expected to replace the pouring type as a green and sustainable cooling and lubrication method [42,43]. Iyappan and Ghosh [44] used sunflower oil for MQL milling aluminum alloy, and the surface finish of the workpiece has been greatly improved. Haq et al. [45] found that the cooling performance of MQL high-pressure gas is insufficient, and the heat collected from the cutting zone is limited, which cannot meet the demand for heat transfer. Li et al. [46] reported a certain gap between MQL high-pressure gas and traditional castable cooling lubrication. Therefore, cooling lubrication needs further exploration. Ni and Zhu [47] studied the machining characteristics of TC4 alloy by using ultrasonic vibration-assisted milling and MQL technology. Jang et al. [48] developed an artificial neural network-based cutting energy reduction parameter optimization method for MQL milling. Zhang et al. [49] demonstrated that NMQL is a way of adding nanoparticles to the base oil of MQL and adding an appropriate amount of dispersant. Nanofluid is prepared after ultrasonic vibration mixing and then atomized at the nozzle using high-pressure gas and spray into the cutting area to play a cooling and lubrication role [50,51]. Gaurav et al. [52] found that MQL reduces the cutting force and surface roughness (35%–47%) within the tool wear range of jojoba oil + nMoS_2 (0.1%), which indicates that jojoba oil, as well as the optimal concentration of jojoba oil and molybdenum disulfide nanoparticles, has become the choice for sustainable processing. Yang et al. [53] found that NMQL not only inherits all the advantages of MQL but also solves the defects of insufficient heat transfer capacity in MQL processing; thus, it improves the processing accuracy and surface quality and integrity of the workpiece, extends the service life of the tool, and reduces the pollution to the environment and the cost of production and manufacturing. Qu et al. [54] investigated the application potential of carbon NMQL by studying the MQL of carbon nanofluid in the grinding of carbon fiber reinforced ceramic matrix composites and proposed a greener and more efficient lubrication method. Gao et al. [55] developed a predictive power model for grinding carbon fiber reinforced polymers with single diamond particles using carbon nanotubes nano lubricants. Gao et al. [56] studied the dispersion mechanism and tribological properties of vegetable oil-based carbon nanotube nanofluids with different surfactants. Therefore, NMQL is expected to replace pouring as a scientific and environmental protection cooling lubrication method.

Most of the existing milling force models are established in the traditional machining, using flood, and dry cooling. Among them, the flood can effectively reduce the milling area temperature. However, the excessive amount of cutting fluid and the cutting fluid spatter negatively affect the health of the machining personnel. At the same time, the direct discharge of untreated waste cutting fluid can cause serious pollution to the environment. The emergence of NMQL to meet the current theme of clean and low-carbon processing has added a new cooling and lubrication method to the processing and manufacturing field. Thus, it solves the problem of environmental pollution caused by casting cooling and lubrication and the technical bottleneck of insufficient heat transfer capacity of MQL. However, the matching mechanical model is less studied. The process of establishing the instantaneous milling force model is deduced by derivation and experiment, and the calculating formula of the milling force coefficients of the spiral end milling cutter is given. The milling force coefficients are obtained by experiments under dry and NMQL, and the instantaneous milling force models are established and verified by experiments. The milling forces measured under dry and NMQL are compared as well.

2 Mechanical behavior analysis

2.1 Instantaneous cutting thickness

Instantaneous milling thickness is an important parameter in the milling force model [57]. In the ideal state, Kline et al. [58] reported that the instantaneous cutting thickness is expressed by the feed speed and the position angle of the microelement (Fig. 1):

$$h = f_z \sin\theta, \tag{1}$$

where h is the instantaneous cutting thickness, f_z is the feed speed, and θ is the angular position of the tooth in the cutting.

2.2 Micro-unit milling force

The instantaneous milling mechanical model is based on Martellotti, and the force is calculated according to the milling load. The micro milling force component can be expressed as the product of the milling micro area and the milling force coefficient.

Figure 2 shows the schematic of micro-unit milling force. The center of the bottom circle of the milling cutter is used as the origin of the coordinates, the x-axis is the feeding direction of the workpiece, the y-axis is determined by the right-handed coordinate system criterion, and the z-axis is the axis direction of the cutter. The spiral edge of the tool is divided into a certain number of microelements with equal spacing along the axial direction, as shown in Fig. 2.

Milling force includes shear force and ploughshare force. Two different milling force coefficients (ploughing and shear force coefficients) are used to represent the milling force, which can be expressed as [59]

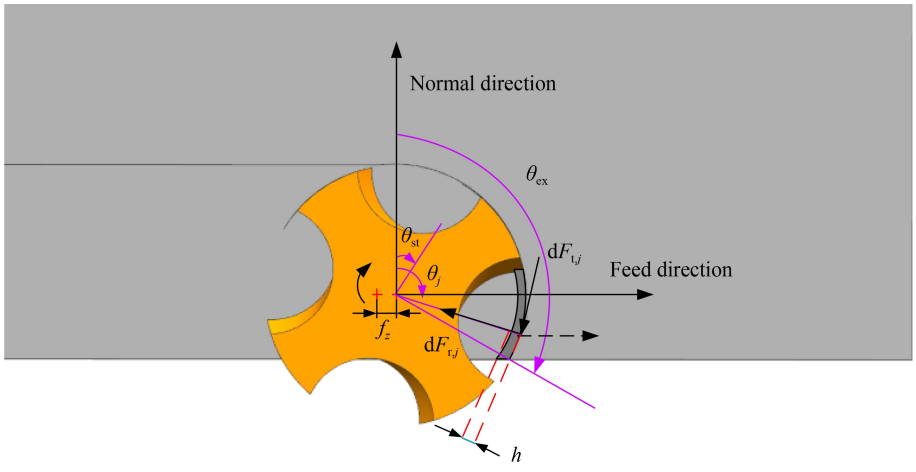

Fig. 1 Schematic of milling thickness.

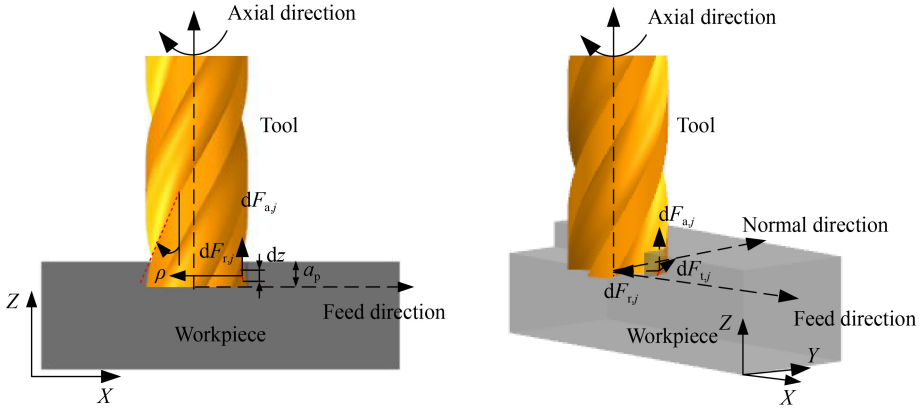

Fig. 2 Schematic of micro-unit milling force.

$$\begin{cases} dF_t = K_{tc}h dz + K_{te} dz, \\ dF_r = K_{rc}h dz + K_{re} dz, \\ dF_a = K_{ac}h dz + K_{ae} dz, \end{cases} \tag{2}$$

where dF_t, dF_r, and dF_a are tangential, radial, and axial forces, respectively, K_{te}, K_{re}, and K_{ae} are tangential, radial, and axial edge ratio coefficients, respectively, dz is the axial cutting height element, and K_{tc}, K_{rc}, and K_{ac} are tangential, radial, and axial shear ratio coefficients, respectively.

Figure 3 shows the diagram of coordinate system transformation. Equation (2) is transformed into rectangular coordinates. The conversion relation is

$$\begin{pmatrix} dF_{x,j}(\theta,z) \\ dF_{y,j}(\theta,z) \\ dF_{z,j}(\theta,z) \end{pmatrix} = \begin{pmatrix} -\cos\theta & -\sin\theta & 0 \\ \sin\theta & -\cos\theta & 0 \\ 0 & 0 & 1 \end{pmatrix} \begin{pmatrix} dF_t \\ dF_r \\ dF_a \end{pmatrix}, \tag{3}$$

where j is the jth cutting tooth, $dF_{x,j}(\theta, z)$, $dF_{y,j}(\theta, z)$, $dF_{z,j}(\theta, z)$ are respectively the the x-, y-, and z-direction forces applied to the jth micro element cutting edge.

Substituting Eqs. (1) and (2) into Eq. (3) yields

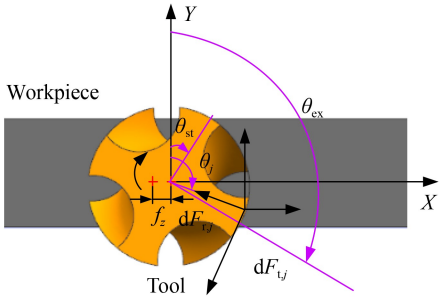

Fig. 3 Schematic of coordinate system transformation.

$$\begin{cases} dF_{x,j}(\theta,z) = -(K_{tc}f_z \sin\theta_j(z) + K_{te})\cos\theta_j(z)dz \\ \qquad\qquad -(K_{rc}f_z \sin\theta_j(z) + K_{re})\sin\theta_j(z)dz, \\ dF_{y,j}(\theta,z) = (K_{tc}f_z \sin\theta_j(z) + K_{te})\sin\theta_j(z)dz \\ \qquad\qquad -(K_{rc}f_z \sin\theta_j(z) + K_{re})\cos\theta_j(z)dz, \\ dF_{z,j}(\theta,z) = (K_{ac}f_z \sin\theta_j(z) + K_{ae})dz, \end{cases} \tag{4}$$

where $\theta_j(z)$ is the instantaneous tooth position angle.

Simplifying Eq. (4) gives

$$\begin{cases} \mathrm{d}F_{x,j}(\theta,z)=\left(\dfrac{f_z}{2}\left(-K_{\mathrm{tc}}\sin(2\theta_j(z))-K_{\mathrm{rc}}\left(1-\cos(2\theta_j(z))\right)\right)+\left(-K_{\mathrm{te}}\cos\theta_j(z)-K_{\mathrm{re}}\sin\theta_j(z)\right)\right)\mathrm{d}z,\\ \mathrm{d}F_{y,j}(\theta,z)=\left(\dfrac{f_z}{2}\left(K_{\mathrm{tc}}\left(1-\cos(2\theta_j(z))\right)-K_{\mathrm{rc}}\sin(2\theta_j(z))\right)+\left(K_{\mathrm{te}}\sin\theta_j(z)-K_{\mathrm{re}}\cos\theta_j(z)\right)\right)\mathrm{d}z,\\ \mathrm{d}F_{z,j}(\theta,z)=\left(K_{\mathrm{ac}}f_z\sin\theta_j(z)+K_{\mathrm{ae}}\right)\mathrm{d}z. \end{cases} \tag{5}$$

The differential milling force is integrated along the force on the jth micro cutting edge to obtain the force model on a single cutting edge for obtaining the total milling force, which can be expressed as

$$F_q(\theta_j(z))=F_q(\theta(z))=\int_{z_{j,1}}^{z_{j,2}}\mathrm{d}F_q(\theta,z),\ q=x,y,z, \tag{6}$$

where $z_{j,1}$ and $z_{j,2}$ are the lower axial meshing limit and upper axial meshing limit of the cutting part of the cutter tooth j, respectively.

The changes in variables are shown in Eqs. (7) and (8):

$$\theta_j(z)=2\pi nt-(j-1)\frac{2\pi}{N}-\frac{2z\tan\rho}{R}\Rightarrow$$

$$\mathrm{d}\theta_j(z)=-\frac{2\tan\rho}{R}\mathrm{d}z, \tag{7}$$

$$\mathrm{d}z=-\frac{R}{2\tan\rho}\mathrm{d}\theta_j(z),\ \begin{cases} z=z_{j,1}\rightarrow\theta_j(z)=\theta_j(z_1),\\ z=z_{j,2}\rightarrow\theta_j(z)=\theta_j(z_2), \end{cases} \tag{8}$$

where n is the spindle speed, t is the milling time, N is the number of milling cutter teeth, ρ is the spiral angle of the milling cutter, and R is the diameter of the tool.

Substituting Eq. (8) into Eq. (6) yields

$$F_q(\theta_j(z))=-\frac{R}{2\tan\rho}\int_{\theta_j(z_1)}^{\theta_j(z_2)}\mathrm{d}F_q(\theta_j(z)),\ q=x,y,z. \tag{9}$$

Substituting Eq. (5) into Eq. (9) yields

$$\begin{cases} F_{x,j}(\theta(z))=-\dfrac{R}{2\tan\rho}\displaystyle\int_{\theta_j(z_1)}^{\theta_j(z_2)}\left(\frac{f_z}{2}\left(-K_{\mathrm{tc}}\sin2\theta_j(z)-K_{\mathrm{rc}}\left(1-\cos2\theta_j(z)\right)\right)+\left(-K_{\mathrm{te}}\cos\theta_j(z)-K_{\mathrm{re}}\sin\theta_j(z)\right)\right)\mathrm{d}\theta,\\ F_{y,j}(\theta(z))=-\dfrac{R}{2\tan\rho}\displaystyle\int_{\theta_j(z_1)}^{\theta_j(z_2)}\left(\frac{f_z}{2}\left(K_{\mathrm{tc}}\left(1-\cos2\theta_j(z)\right)-K_{\mathrm{rc}}\sin2\theta_j(z)\right)+\left(K_{\mathrm{te}}\sin\theta_j(z)-K_{\mathrm{re}}\cos\theta_j(z)\right)\right)\mathrm{d}\theta,\\ F_{z,j}(\theta(z))=-\dfrac{R}{2\tan\rho}\displaystyle\int_{\theta_j(z_1)}^{\theta_j(z_2)}\left(K_{\mathrm{ac}}f_z\sin\theta_j(z)+K_{\mathrm{ae}}\right)\mathrm{d}\theta. \end{cases} \tag{10}$$

Sorting out Eq. (10) gives

$$\begin{cases} F_{x,j}(\phi(\mathrm{z}))=\left(-\dfrac{Rf_z}{8\tan\rho}\left(K_{\mathrm{tc}}\cos(2\theta_j(z))-K_{\mathrm{rc}}\left(2\theta_j(z)-\sin(2\theta_j(z))\right)\right)+\dfrac{R}{2\tan\rho}\left(K_{\mathrm{te}}\sin\theta_j(z)-K_{\mathrm{re}}\cos\theta_j(z)\right)\right)_{\theta_j(z_1)}^{\theta_j(z_2)},\\ F_{y,j}(\phi(\mathrm{z}))=\left(-\dfrac{Rf_z}{8\tan\rho}\left(K_{\mathrm{tc}}\left(2\theta_j(z)-\sin(2\theta_j(z))\right)-K_{\mathrm{rc}}\cos(2\theta_j(z))\right)+\dfrac{R}{2\tan\rho}\left(K_{\mathrm{te}}\cos\theta_j(z)+K_{\mathrm{re}}\sin\theta_j(z)\right)\right)_{\theta_j(z_1)}^{\theta_j(z_2)},\\ F_{z,j}(\theta(z))=\left(\dfrac{Rf_z}{2\tan\rho}\left(K_{\mathrm{ac}}\cos\theta_j(z)+\dfrac{R}{2\tan\rho}K_{\mathrm{ae}}\theta_j(z)\right)\right)_{\theta_j(z_1)}^{\theta_j(z_2)}. \end{cases} \tag{11}$$

The hysteresis angle of all axial cutting depths is calculated by Eq. (12):

$$\psi_{\mathrm{a}}=\frac{2\tan\rho}{R}a_{\mathrm{p}}, \tag{12}$$

where ψ_{a} is the lag angle at the maximum axial cutting depth, and a_{p} is the axial cutting depth.

As shown in Fig. 3, the milling force exists only when the cutter is in the milling area, which can be expressed as Eq. (13):

$$\theta_{\mathrm{st}}\leqslant\theta_j\leqslant\theta_{\mathrm{ex}}+\psi_a, \tag{13}$$

$$\begin{cases} \theta_{\mathrm{st}}=\pi-\arccos\dfrac{R-a_{\mathrm{p}}}{R}\\ \theta_{\mathrm{ex}}=\pi \end{cases}\Rightarrow(\mathrm{down}), \tag{14}$$

$$\begin{cases}\theta_{st}=\pi\\ \theta_{ex}=\pi-\arccos\dfrac{R-a_p}{R}\end{cases}\Rightarrow(\text{up}),\tag{15}$$

where θ_{st} is the cutter entry angle, θ_{ex} is the cutter exit angle, and θ_j is the instantaneous tooth position angle of the jth slot.

The boundary conditions for calculating the milling force of each round of milling cutter are shown in Fig. 4 and can be expressed as Eq. (16):

$$\begin{cases}\text{If } \theta_j<\theta_{st} \text{ or } \theta_j>\theta_{ex}+\psi_a \Rightarrow \text{out of cut: } F_{(x,y,z)}(j)=0,\\ \text{If } \theta_{st}<\theta_j<\theta_{st}+\psi_a \Rightarrow \text{cutting}\begin{cases}\theta_j(z_1)=\theta_{st},\\ \theta_j(z_2)=\theta_j,\end{cases}\\ \text{If } \theta_{st}+\psi_a<\theta_j<\theta_{ex} \Rightarrow \text{cutting}\begin{cases}\theta_j(z_1)=\theta_j-\psi_a,\\ \theta_j(z_2)=\theta_j,\end{cases}\\ \text{If } \theta_{ex}<\theta_j<\theta_{ex}+\psi_a \Rightarrow \text{cutting}\begin{cases}\theta_j(z_1)=\theta_j-\psi_a,\\ \theta_j(z_2)=\theta_{ex}.\end{cases}\end{cases}\tag{16}$$

In combination with Eq. (16) and Fig. 3, the cutting process can be divided into four states according to the expansion patterns of various cutting states and the positions of the cutting angle θ_{st} and the cutting angle θ_{ex}:

(1) When $\theta_j < \theta_{st}$ or $\theta_j > \theta_{ex} + \psi_a$, the cutting edge cannot cut the workpiece. θ_{st} and the cutting angle θ_{ex} are also 0. Thus, the cutting force is 0.

(2) When $\theta_{st} < \theta_j < \theta_{st} + \psi_a$, the cutting state is shown in Fig. 3. Owing to the lag angle, the milling cutter gradually cuts into the workpiece from the bottom of the cutting edge until the cutting height no longer increases. The cut angle $\theta_j = \theta_{st}$, and the cut angle $\theta_{ex} = \theta_j$.

(3) When $\theta_{st} + \psi_a < \theta_j < \theta_{ex}$, the cutting state is at the entire axial cutting depth, and all the cutting elements involved in the cutting are cutting the workpiece. The entry angle is $\theta_j = \psi_a$, and the exit angle $\theta_{ex} = \theta_j$.

(4) When $\theta_{ex} < \theta_j < \theta_{ex} + \psi_a$, the cutting edge of the milling cutter gradually cuts out the workpiece from the bottom. However, the cutting edge does not directly cut out the workpiece owing to the lag angle, but the cutting height gradually decreases. The cut angle is $(\theta_j - \psi_a)$, and the cut angle $\theta_{ex} = \theta_j$.

2.3 Milling force coefficient

In this study, a mechanical method for fast calibration of the milling cutter is presented. Under the condition of constant contact angle and axial cutting depth, a group of milling experiments are conducted by changing the feed rate only, and the average force of each cutter tooth cycle is measured. The total cutting force per revolution of the spindle needs to be measured and divided by the number of cutter teeth. $\theta_j(z) = \theta$ are substituted into Eq. (5), and the integral within the first rotation of the principal axis is divided by tooth spacing angle ($\theta_p = 2\pi/N$). The average milling force per tooth cycle is obtained as follows:

$$\overline{F}_q=-\frac{1}{\theta_p}\int_{\theta_{st}}^{\theta_{ex}}\mathrm{d}F_q(\theta),\ q=x,y,z,\tag{17}$$

where $\overline{F}_q$ is the periodic average milling force per tooth, and θ_p is the angle between teeth of milling cutter.

The spiral groove is only cut in the contact area ($\theta_{st} \leqslant \theta \leqslant \theta_{ex}$).

After integration, the instantaneous cutting force is obtained as follows:

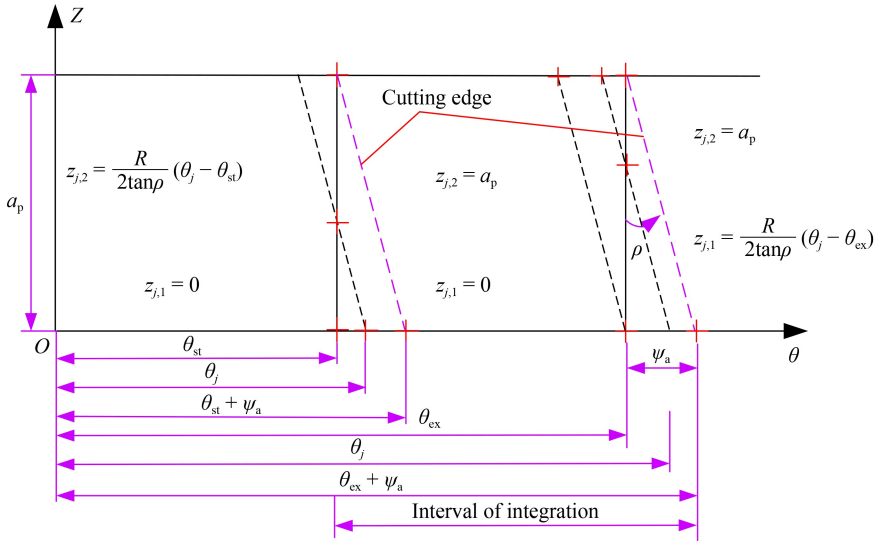

Fig. 4 Boundary conditions of milling force model.

$$\begin{cases} \overline{F}_x = \left(\dfrac{Na_p f_z}{8\pi} (K_{tc}\cos(2\theta) - K_{rc}(2\theta - \sin(2\theta))) + \dfrac{Na_p}{2\pi} (-K_{te}\sin\theta + K_{re}\cos\theta) \right)_{\theta_{st}}^{\theta_{ex}}, \\ \overline{F}_y = \left(\dfrac{Na_p f_z}{8\pi} (K_{tc}(2\theta - \sin(2\theta)) + K_{rc}\cos(2\theta)) - \dfrac{Na_p}{2\pi} (K_{te}\cos\theta + K_{re}\sin\theta) \right)_{\theta_{st}}^{\theta_{ex}}, \\ \overline{F}_z = \left(\dfrac{Na_p}{2\pi} (-K_{ac} f_z \cos\theta + K_{ae}\theta) \right)_{\theta_{st}}^{\theta_{ex}}. \end{cases} \tag{18}$$

Slot milling experiment is the most convenient. At this time, the cut angle $\theta_{st} = 0$ and the cut angle $\theta_{ex} = \pi$. By substituting them into Eq. (18), the average milling force per tooth in a cycle can be simplified as

$$\begin{cases} \overline{F}_x = -\dfrac{Na_p}{4} K_{rc} f_z - \dfrac{Na_p}{\pi} K_{re}, \\ \overline{F}_y = \dfrac{Na_p}{4} K_{tc} f_z + \dfrac{Na_p}{\pi} K_{te}, \\ \overline{F}_z = \dfrac{Na_p}{4} K_{ac} f_z + \dfrac{Na_p}{\pi} K_{ae}. \end{cases} \tag{19}$$

The average milling force can be expressed as the sum of the linear function of the feed rate f_z per tooth and the cutting force:

$$\overline{F}_q = \overline{F}_{qc} f_z + \overline{F}_{qe}, \quad q = x, y, z, \tag{20}$$

where $\overline{F}_{qe}$ is the coefficient component of cutting edge force, and $\overline{F}_{qc}$ is the component of cutting edge force.

The average milling force at different feed rates is measured, and the average milling force coefficient is obtained by linear regression. According to Eqs. (19) and (20), the cutting force coefficient can be obtained as follows:

$$\begin{aligned} K_{tc} &= \frac{4\overline{F}_{yc}}{Na_p}, \; K_{te} = \frac{\pi \overline{F}_{ye}}{Na_p}, \\ K_{rc} &= \frac{-4\overline{F}_{xc}}{Na_p}, \; K_{re} = \frac{-\pi \overline{F}_{xe}}{Na_p}, \\ K_{ac} &= \frac{\pi \overline{F}_{zc}}{Na_p}, \; K_{ae} = \frac{2\overline{F}_{ze}}{Na_p}. \end{aligned} \tag{21}$$

The calculated coefficient value is substituted into Eq. (11).

2.4 Instantaneous milling force model

Effects of discontinuous cutting during milling are determined by

$$A(\theta) = \begin{cases} 1, & \theta_{st} \leqslant \theta_j \leqslant \theta_{ex} + \psi_a, \\ 0, & \text{other}, \end{cases} \tag{22}$$

where $A(\theta)$ is used to determine whether the tool is involved in cutting.

When the milling cutter is involved in cutting, the contribution to the force of the milling cutter is 1; otherwise, it is 0. By using Eq. (23), the predicted milling force is summarized.

$$\begin{cases} F_x = \sum_{j=1}^{N} A(\theta) F_{x,j}(\theta_j), \\ F_y = \sum_{j=1}^{N} A(\theta) F_{y,j}(\theta_j), \\ F_z = \sum_{j=1}^{N} A(\theta) F_{z,j}(\theta_j). \end{cases} \tag{23}$$

3 Experimental verification

3.1 Experimental equipment

The milling experiment is conducted on the computerized numerical control (CNC) machine tool ML1060B. The MQL supply uses the Jinzhao KS-2106, and JR-YDCL-III05B three-way force measuring system is used to collect milling force. Figure 5 shows the experimental equipment.

3.2 Experimental material

The workpiece size used in the experiment is 100 mm × 100 mm × 40 mm. The material is aerospace aluminum alloy 7050. The chemical composition and performance parameters of 7050 aluminum alloy are listed in Tables 1 and 2, respectively.

Duan et al. [60] and Zhao et al. [61] analyzed Al_2O_3 nanofluids, and the nanofluids are proportioned with cottonseed oil and Al_2O_3 nanoparticles. Table 3 lists the characteristics of cotton oil. Table 4 shows the fatty acid composition of cottonseed oil. Table 5 lists the physical properties of Al_2O_3 nanoparticles.

Cutting tools use SGO four-edge end milling cutter S550 with a size of 12 × 12D × 36C × 75L, where D represents the diameter of the milling cutter shank, C represents the cutting edge length of the milling cutter, and L represents the total length of the milling cutter.

3.3 Experimental condition

Yang et al. [62] confirmed that nanofluid has a better

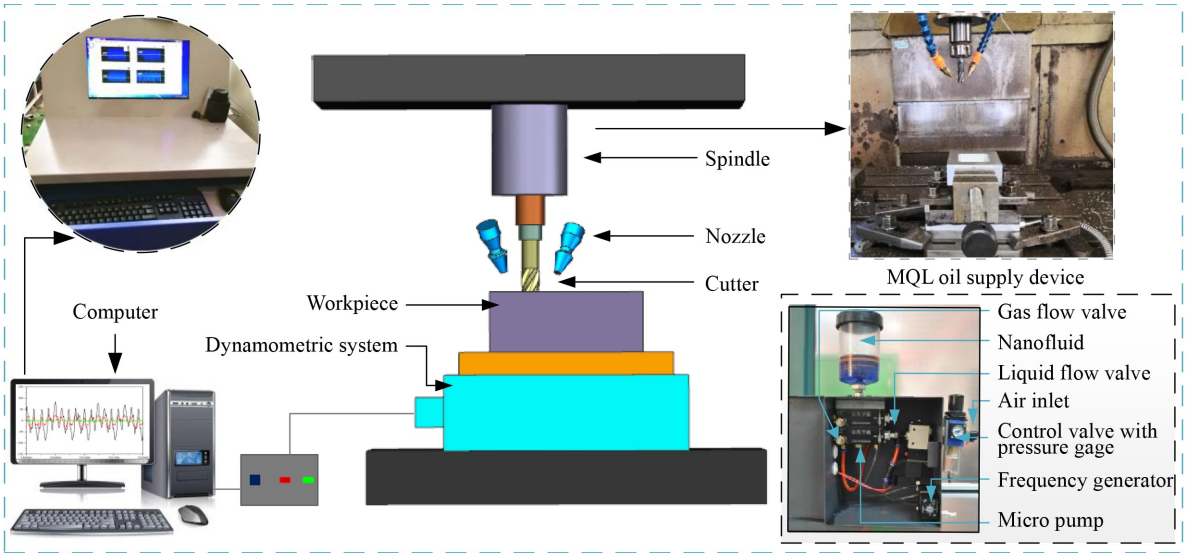

Fig. 5 Experimental equipment of aerospace aluminum alloy milling force.

Table 1 Chemical composition of workpieces

Element	Mass percentage/wt.%
Al	Margin
Cr	⩽ 0.04
Zr	0.08–0.15
Zn	5.70–6.70
Si	⩽ 0.12
Fe	0.00–0.15
Mn	⩽ 0.10
Mg	1.90–2.60
Ti	⩽ 0.12
Cu	1.90–2.60

Table 2 Mechanical properties of workpieces

Tensile strength	Yield strength	Hardness	Elongation	Density
552 MPa	489 MPa	140 HB	11%	2.83 g/cm^3

effect when the concentration of nanoparticles is 0.5 wt.% and the concentration of dispersant (SDS) is 0.3 wt.%. As shown in Fig. 6, a certain amount of nanoparticles, cottonseed oil, and dispersant are weighed by an electronic balance. After the nanoparticles are proportioned using cottonseed oil and disperser, they are stirred with a blender for 15 min and placed in the ultrasonic vibration instrument for 60 min [63,64].

3.4 Experimental design and data preprocessing

SGO four-edge end milling cutter S550 with a size of 12 × 12D × 36C × 75L is utilized. Tables 6 and 7 are the experimental milling parameters [65,66].

The sample frequency of force measurement in the experiment is 30000 Hz. Three groups of data are sampled under each working condition to ensure the authenticity of the sampled data.

The experimental data are analyzed and calculated, and the milling forces are measured for three times at the feed

Table 3 Characteristics of cottonseed oil

Temperature/°C	Density/(g·cm^{-3})	Refractive index	Iodine value/g	Flash point/°C	Freezing point/°C	Saponification value	Viscosity/(mPa·s)
20	0.92	1.46–1.47	99–113	324	5	191–199	50.6
30	0.93	1.46–1.47	99–113	324	5	191–199	27.9

Table 4 Fatty acid of cottonseed oil

Myristic acid	Palmitic acid	Octadecenoic acid	Linoleic acid	Stearic acid	Linolenic acid	Other
0.6%–1.0%	21.4%–26.4%	18.0%–30.7%	44.9%–55.0%	2.1%–3.3%	0.4%	0.3%–1.8%

Table 5 Properties of Al_2O_3 nanoparticles

Shape	Purity	Average particle size	Apparent density	Specific surfacearea	Heat conductivity coefficient
Spheroidal	99.9%	70 nm	0.33 g/cm^3	30.21 m^2/g	40 W·m^{-1}·K^{-1}

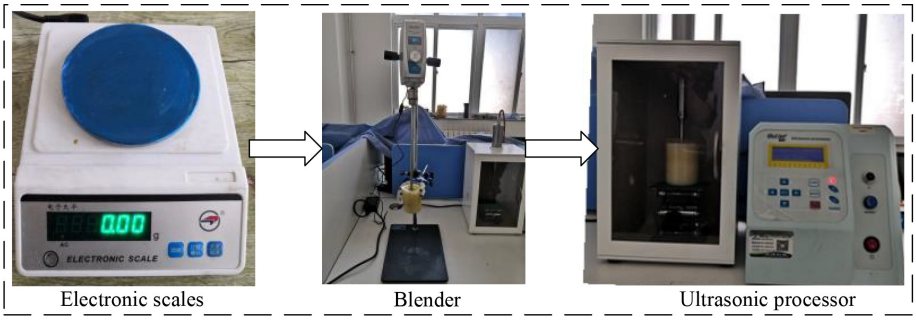

Fig. 6 Nanofluid preparation equipment for milling force experiment.

Table 6 Experimental milling parameters

Parameters	Numerical value
Milling mode	Climb cutting
Flow rate of NMQL	50 mL/h
Distance of NMQL	30 mm
Nozzle elevation	60°
Nozzle incidence angle	35°
Air pressure	0.4 MPa

Table 7 Test parameters for milling force coefficient identification

No.	Spindle speed, n/(r·min^{-1})	Axial cutting depth, a_p/mm	Feed speed, f_z/(mm·min^{-1})
1	2000	1	200
2	2000	1	300
3	2000	1	400

rate of each tooth. The average of the three milling forces is taken to obtain the average milling forces in x-, y-, and z-axis in Table 8, and the milling force coefficients are calculated by Eqs. (20) and (21), as shown in Table 9.

3.5 Numerical analysis

Numerical simulation flowchart for milling force is shown in Fig. 7. Increment step length is determined according to the milling cutter rotation angle, and the blade of a location is determined at the end of each simulation step size. Whether the radial contact angle between the entrance angle and cut out angle is involved in cutting is determined. The corresponding cutting thickness is calculated, and the micro-unit on the tangential, radial, and axial forces is obtained. The milling force in each step length is the total force of all

Table 8 Experimental result of milling force

No.	NMQL			Dry		
	$\overline{F_x}$/N	$\overline{F_y}$/N	$\overline{F_z}$/N	$\overline{F_x}$/N	$\overline{F_y}$/N	$\overline{F_z}$/N
1	42.40	−51.05	−26.42	61.57	−69.91	−31.19
2	59.79	−73.02	−38.24	80.42	−88.79	−42.95
3	78.28	−89.42	−50.12	99.11	−104.42	−55.32

the cutter teeth participating in milling simultaneously.

Figures 8(a) and 8(b) verify the milling results of aerospace aluminum alloy under dry and NMQL. The milling force waveform in Fig. 8 shows that the measured value is in a stable fluctuation state, while the calculated value does not fluctuate, and the two data fit well. Under dry milling, the average absolute errors of the force model are 2.5%, 9.9%, and 4.4% in the x-, y-, and z-direction, respectively.

Figures 8(c) and 8(d) verify the milling results of aerospace aluminum alloy under NMQL. The milling force waveform in Fig. 8(c) shows that the measured value is in a stable fluctuation state, while the calculated value does not fluctuate, and the two data fit well. The average absolute errors of milling force prediction in the x-, y-, and z-direction are 13.3%, 2.3%, and 7.6%, respectively. In addition, the force model can predict the change in milling force with tool rotation.

Figure 9 shows the comparison of dry and NMQL milling forces. The comparison of experimental milling forces obtained under dry and NMQL shows that the milling forces measured under NMQL in the x-, y-, and z-direction decrease by 21.4%, 17.7%, and 18.5%, respectively.

Figure 10 shows that Al_2O_3 has a hexagonal precise accumulation of molecular structure, which enables it to have good wear resistance, hardness, and heat resistance.

Table 9 Instantaneous milling force coefficients

Cooling mode	K_{tc}/(N·mm^{-2})	K_{rc}/(N·mm^{-2})	K_{ac}/(N·mm^{-2})	K_{te}/(N·mm^{-1})	K_{re}/(N·mm^{-1})	K_{ae}/(N·mm^{-1})
Dry	−1380.4	−1501.2	−757.68	−27.79	−18.87	−3.35
NMQL	−1534.8	−1435.2	−742.59	−9.95	−5.12	−1.36

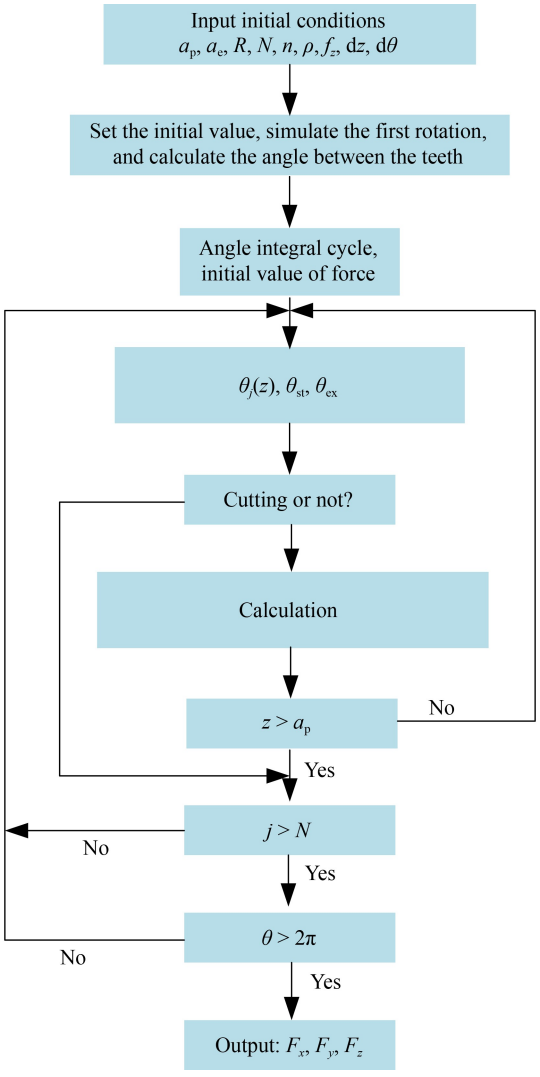

Fig. 7 Flowchart of instantaneous milling force simulation.

Al_2O_3 nanoparticles are spherical for the most part. Thus, they can prevent direct contact of friction pairs and improve the bearing capacity and extreme-pressure performance of lubricating oil. They can also serve as a "protective oil film." The size of Al_2O_3 nanoparticles used in this experiment is very small (particle size ⩽ 70 nm), which can easily enter sliding contact without disturbing the hydrodynamic state. When Al_2O_3 nanoparticles are added to the lubricating oil, they can easily enter the milling area because of the compression stress of the lubricating oil. A self-composite film is then formed, which creates a micro-polish that can self-repair the rubbing surface. Ultimately, a "filling effect" is generated. The added Al_2O_3 nanoparticles serve as the hard phase of lubricating oil (HR = 2700–3000). Thus, the friction process can show excellent wear resistance. More cutting fluid can be attached to the surface because of the strong adsorption capacity of the Al_2O_3 molecular structure. This phenomenon can improve the total amount of nanofluids transported to the interface of tool/workpiece and tool/chip. Then, more lubricating oil film can be formed to reduce friction and anti-wear [67–69].

The proportion of saturated fatty acids in cottonseed oil is higher than 27%, 24.8% of which is palmitic acid and 2.4% of which is stearic acid. The binding energy between the workpiece surface and the saturated fatty acid is the largest. Thus, the adsorbed oil film is strong and stable. Cottonseed oil also contains oleic acid, with a content of 25% [70]. In general, the cottonseed oil contains more saturated fatty acids; thus, it contains more polar molecules and has greater binding energy with the surface of the workpiece [71–73]. The strength of the oil film formed is high, and the oil film of greater density and strength can be achieved. The persistence of the oil film formed is good as well. Therefore, cottonseed oil has excellent lubricating properties.

4 Conclusions

The milling force modeling of the whole end milling cutter milling process was conducted using the instantaneous milling force model. The milling thickness model and the micro milling force model were calculated and deduced, respectively, and the average milling force coefficient model of the whole end milling cutter was established to solve the milling force coefficient in the nanometer fluid micro lubrication condition. The specific contents are as follows:

(1) The instantaneous milling force models of dry and NMQL based on the rake face of blade surface plough cut after shear effect and effect mechanism of double integral are set up. The NMQL and milling feeding factor are introduced into the instantaneous milling force coefficient of single factor experiment. In the end, the variation trend of instantaneous milling force is obtained.

(2) The coefficients of milling force model are deduced. Numerical simulation values are compared with the experimental values through the milling experiment of NMQL for calculation and using MATLAB. Both comparisons show that, under dry milling, the average absolute errors of the force model are 2.5%, 9.9%, and 4.4% in the x-, y-, and z-direction, respectively. Under NMQL, the average absolute errors of milling force prediction in the x-, y-, and z-direction are 13.3%, 2.3%, and 7.6%, respectively. The instantaneous milling force model can predict the variation in cutting force with tool rotation.

(3) The comparison of experimental milling forces obtained under dry and NMQL shows that the milling forces measured under NMQL in the x-, y-, and z-direction decrease by 21.4%, 17.7%, and 18.5%, respectively.

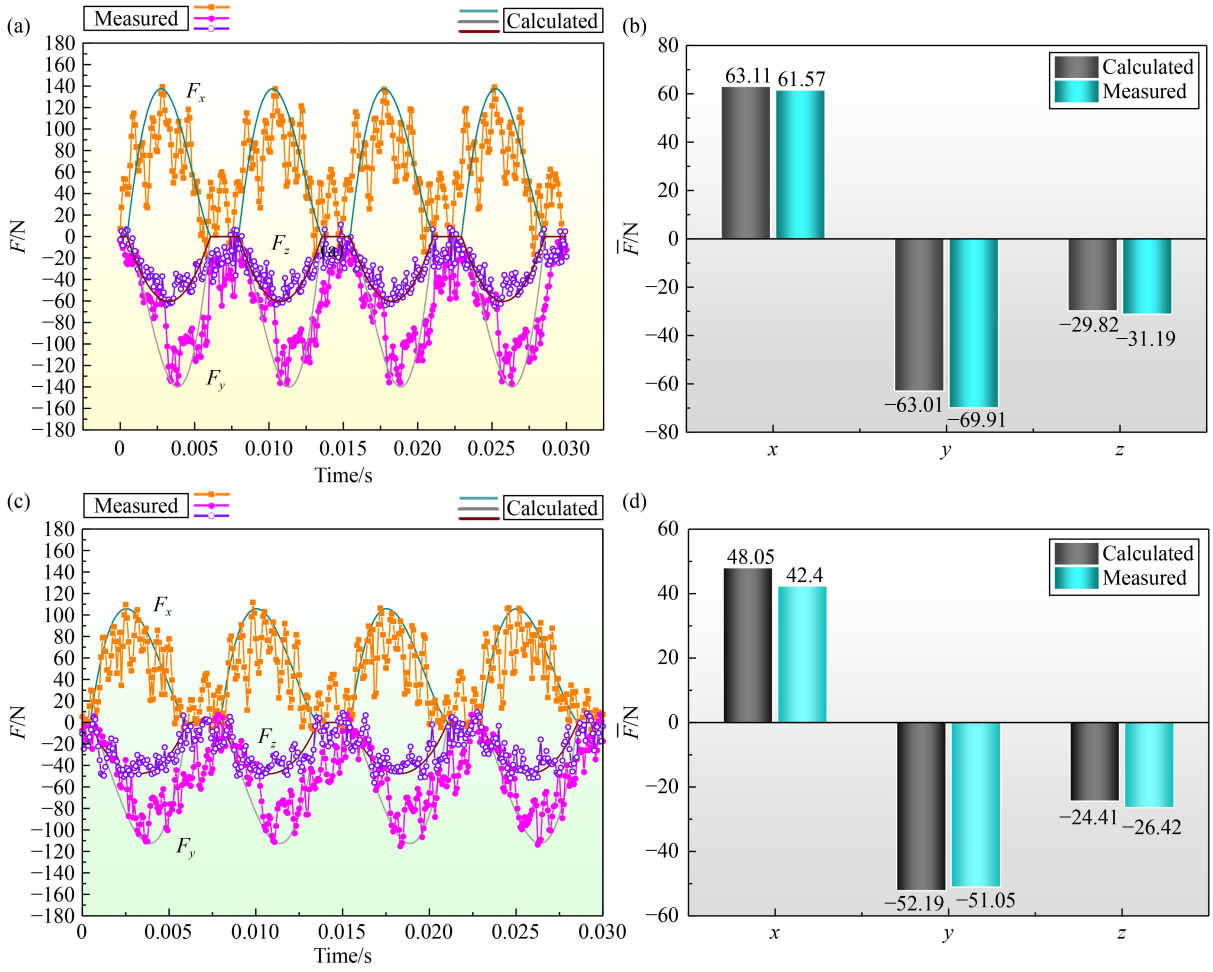

Fig. 8 Comparison of calculated and measured milling forces: (a) dry milling force waveform, (b) dry average milling force, (c) nanofluid minimal quantity lubrication milling force waveform, and (d) nanofluid minimal quantity lubrication average milling force.

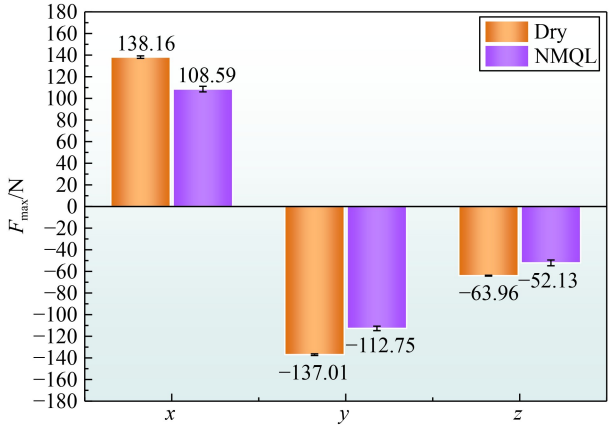

Fig. 9 Comparison of dry and NMQL milling forces. NMQL: nanofluid minimal quantity lubrication.

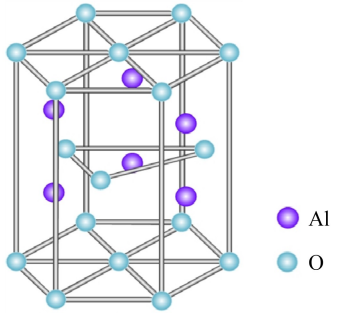

Fig. 10 Schematic of the molecular structure of Al_2O_3 nanoparticles.

Nomenclature

a_p	Axial cutting depth
$A(\theta)$	Determining whether the tool is involved in cutting
f_z	Feed speed
$\overline{F}_q$	Periodic average milling force per tooth
$\overline{F}_{qc}$	Coefficient component of cutting edge force
$\overline{F}_{qe}$	Component of cutting edge force
dF_a	Axial force
dF_r	Radial force

dF_t	Tangential force
$dF_{x,j}(\theta, z)$, $dF_{y,j}(\theta, z)$, $dF_{z,j}(\theta, z)$	x-, y-, and z-direction forces applied to the jth micro element cutting edge, respectively
h	Instantaneous cutting thickness
j	jth cutting tooth
K_{ac}	Axial shearing force coefficient
K_{ae}	Axial edge force coefficient
K_{rc}	Radial shearing force coefficient
K_{re}	Radial edge force coefficient
K_{tc}	Tangential shearing force coefficient
K_{te}	Tangential edge force coefficient
n	Spindle speed
N	Number of milling cutter teeth
R	Diameter of the tool
t	Milling time
$z_{j,1}$	Lower axial meshing limit of the cutting part of the cutter tooth j
$z_{j,2}$	Upper axial meshing limit of the cutting part of the cutter tooth j
dz	Axial cutting height element
θ	Angular position of the tooth in the cutting
θ_{ex}	Cutter exit angle
θ_j	Instantaneous tooth position angle of the jth slot
$\theta_j(z)$	Instantaneous tooth position angle
θ_p	Angle between teeth of milling cutter
θ_{st}	Cutter entry angle
ρ	Spiral angle of the milling cutter
ψ_a	Lag angle at the maximum cutting axial depth

Acknowledgements This study was financially supported by the National Natural Science Foundation of China (Grant Nos. 51975305, 51905289, 52105457, and 52105264), the National Key R&D Program of China (Grant No. 2020YFB2010500), the Key Projects of Shandong Natural Science Foundation, China (Grant Nos. ZR2020KE027, ZR2020ME158, and ZR2021QE116), the Major Science and Technology Innovation Engineering Projects of Shandong Province, China (Grant No. 2019JZZY020111), the Source Innovation Project of Qingdao West Coast New Area, China (Grant Nos. 2020-97 and 2020-98).

References

1. Wahab M A, Park J H, Alam M S, Pang S S. Effect of corrosion prevention compounds on fatigue life in 2024-T3 aluminum alloy. Journal of Materials Processing Technology, 2006, 174(1–3): 211–217
2. Oguri K. Fatigue life enhancement of aluminum alloy for aircraft by fine particle shot peening (FPSP). Journal of Materials Processing Technology, 2011, 211(8): 1395–1399
3. Yang Y Y, Gong Y D, Li C H, Wen X L, Sun J Y. Mechanical performance of 316 L stainless steel by hybrid directed energy deposition and thermal milling process. Journal of Materials Processing Technology, 2020, 291: 117023
4. Yuan J L, Lyu B H, Hang W, Deng Q F. Review on the progress of ultra-precision machining technologies. Frontiers of Mechanical Engineering, 2017, 12(2): 158–180
5. Qi H, Qin S K, Cheng Z C, Zou Y L, Cai D H, Wen D H. DEM and experimental study on the ultrasonic vibration-assisted abrasive finishing of WC-8Co cemented carbide cutting edge. Powder Technology, 2021, 378: 716–723
6. Qu S S, Yao P, Gong Y D, Yang Y Y, Chu D K, Zhu Q S. Modelling and grinding characteristics of unidirectional C–SiCs. Ceramics International, 2022, 48(6): 8314–8324
7. Chen X Z, Li C B, Tang Y, Li L, Li H C. Energy efficient cutting parameter optimization. Frontiers of Mechanical Engineering, 2021, 16(2): 221–248
8. Qin C J, Tao J F, Shi H T, Xiao D G, Li B C, Liu C L. A novel Chebyshev-wavelet-based approach for accurate and fast prediction of milling stability. Precision Engineering, 2020, 62: 244–255
9. Huang Z W, Zhu J N, Lei J T, Li X R, Tian F Q. Tool wear predicting based on multi-domain feature fusion by deep convolutional neural network in milling operations. Journal of Intelligent Manufacturing, 2020, 31(4): 953–966
10. Li X, Zhao W, Li L, He N, Chi S W. Modeling and application of process damping in milling of thin-walled workpiece made of titanium alloy. Shock and Vibration, 2015, 431476
11. Jiang X H, Kong X J, He S R, Wu K. Modeling the superposition of residual stresses induced by cutting force and heat during the milling of thin-walled parts. Journal of Manufacturing Processes, 2021, 68: 356–370
12. Niccolò G, Lorenzo M, Antonio S, Gianni C. A frequency-based analysis of cutting force for depths of cut identification in peripheral end-milling. Mechanical Systems and Signal Processing, 2022, 171: 108943
13. Song Y, Qu D, Wu B, Cao H J. Composite light ropes model-based dynamics force prediction model of high speed dry milling UD-CF/PEEK considering size effect. Journal of Manufacturing Processes, 2022, 76: 210–222
14. Liao Z R, Axinte D, Gao D. On modelling of cutting force and temperature in bone milling. Journal of Materials Processing Technology, 2019, 266: 627–638
15. Farhadmanesh M, Ahmadi K. Online identification of mechanistic milling force models. Mechanical Systems and Signal Processing, 2021, 149: 107318
16. Zheng L, Chiou Y S, Liang S Y. Three dimensional cutting force analysis in end milling. International Journal of Mechanical Sciences, 1996, 38(3): 259–269
17. Yun W S, Cho D W. Accurate 3-D cutting force prediction using cutting condition independent coefficients in end milling. International Journal of Machine Tools and Manufacture, 2001, 41(4): 463–478
18. Desai K A, Agarwal P K, Rao P V M. Process geometry modeling with cutter runout for milling of curved surfaces. International Journal of Machine Tools and Manufacture, 2009, 49(12–13): 1015–1028

19. Montgomery D, Altintas Y. Mechanism of cutting force and surface generation in dynamic milling. Journal of Engineering for Industry, 1991, 113(2): 160–168
20. Rao V S, Rao P V M. Effect of workpiece curvature on cutting forces and surface error in peripheral milling. Proceedings of the Institution of Mechanical Engineers, Part B: Journal of Engineering Manufacture, 2006, 220(9): 1399–1407
21. Koenigsberger F, Sabberwal A J P. An investigation into the cutting force pulsations during milling operations. International Journal of Machine Tool Design and Research, 1961, 1(1–2): 15–33
22. Sutherland J W, DeVor R E. An improved method for cutting force and surface error prediction in flexible end milling systems. Journal of Engineering for Industry, 1986, 108(4): 269–279
23. Budak E, Altintas Y. Peripheral milling conditions for improved dimensional accuracy. International Journal of Machine Tools and Manufacture, 1994, 34(7): 907–918
24. Armarego E J A, Whitfield R. C. Computer based modelling of popular machining operations for force and power prediction. CIRP Annals, 1985, 34(1): 65–69
25. Davoudinejad A, Parenti P, Annoni M. 3D finite element prediction of chip flow, burr formation, and cutting forces in micro end-milling of aluminum 6061-T6. Frontiers of Mechanical Engineering, 2017, 12(2): 203–214
26. Altintas Y. Manufacturing Automation: Metal Cutting Mechanics, Machine Tool Vibrations, and CNC Design. 2nd ed. Cambridge: Cambridge University Press, 2012
27. Chen Y H, Lu J, Deng Q L, Ma J Y, Liao X P. Modeling study of milling force considering tool runout at different types of radial cutting depth. Journal of Manufacturing Processes, 2022, 76: 486–503
28. Wang C X, Zhang X W, Zhai Z, Chen X F. Parametric prediction model and periodic fluctuation interpretation of unidirectional CFRP edge milling force. Composite Structures, 2022, 287: 115387
29. Wang F J, Li Y, Zhang B Y, Deng J, Lin Y Q, Yang L L, Fu R. Theoretical model of instantaneous milling force for CFRP milling with a ball-end milling cutter: considering spatial dimension and temporal dimension discontinuity effects. Journal of Manufacturing Processes, 2022, 75: 346–362
30. Arnaud L, Gonzalo O, Seguy S, Jauregi H, Peigné G. Simulation of low rigidity part machining applied to thin-walled structures. The International Journal of Advanced Manufacturing Technology, 2011, 54(5): 479–488
31. Zaghbani I, Songmene V. A force-temperature model including a constitutive law for dry High speed milling of aluminium alloys. Journal of Materials Processing Technology, 2009, 209(5): 2532–2544
32. Merdol S D. Mechanics and dynamics of serrated end mills. Thesis for the Master's Degree. Vancouver: University of British Columbia, 2003
33. Gradišek J, Kalveram M, Weinert K. Mechanistic identification of specific force coefficients for a general end mill. International Journal of Machine Tools and Manufacture, 2004, 44(4): 401–414
34. Wan M, Pan W J, Zhang W H, Ma Y C, Yang Y. A unified instantaneous cutting force model for flat end mills with variable geometries. Journal of Materials Processing Technology, 2014, 214(3): 641–650
35. Sun T, Qin L F, Fu Y C, Liu C Q, Shi R L. Mathematical modeling of cutting layer geometry and cutting force in orthogonal turn-milling. Journal of Materials Processing Technology, 2021, 290: 116992
36. Cai S J, Cai Z Q, Yao B, Shen Z H, Ma X F. Identifying the transient milling force coefficient of a slender end-milling cutter with vibrations. Journal of Manufacturing Processes, 2021, 67: 262–274
37. Coz G L, Marinescu M, Devillez A, Dudzinski D, Velnom L. Measuring temperature of rotating cutting tools: application to MQL drilling and dry milling of aerospace alloys. Applied Thermal Engineering, 2012, 36: 434–441
38. Bruni C, Forcellese A, Gabrielli F, Simoncini M. Effect of the lubrication-cooling technique, insert technology and machine bed material on the workpart surface finish and tool wear in finish turning of AISI 420B. International Journal of Machine Tools and Manufacture, 2006, 46(12–13): 1547–1554
39. Yang M, Li C H, Luo L, Li R Z, Long Y Z. Predictive model of convective heat transfer coefficient in bone micro-grinding using nanofluid aerosol cooling. International Communications in Heat and Mass Transfer, 2021, 125: 105317
40. Yang M, Li C H, Zhang Y B, Jia D Z, Li R Z, Hou Y L, Cao H J, Wang J. Predictive model for minimum chip thickness and size effect in single diamond grain grinding of zirconia ceramics under different lubricating conditions. Ceramics International, 2019, 45(12): 14908–14920
41. Zhang X P, Li C H, Zhang Y B, Wang Y G, Li B K, Yang M, Guo S M, Liu G T, Zhang N Q. Lubricating property of MQL grinding of Al_2O_3/SiC mixed nanofluid with different particle sizes and microtopography analysis by cross-correlation. Precision Engineering, 2017, 47: 532–545
42. Wang X M, Li C H, Zhang Y B, Ding W F, Yang M, Gao T, Cao H J, Xu X F, Wang D Z, Zafar S, Debnath S, Jamil M, Ali H M. Vegetable oil-based nanofluid minimum quantity lubrication turning: academic review and perspectives. Journal of Manufacturing Processes, 2020, 59: 76–97
43. Wang X M, Li C H, Zhang Y B, Zafar S, Debnath S, Sharma S, Yang M, Gao T. Influence of texture shape and arrangement on nanofluid minimum quantity lubrication turning. The International Journal of Advanced Manufacturing Technology, 2022, 119(1): 631–646
44. Iyappan S K, Ghosh A. Small quantity lubrication assisted end milling of aluminium using sunflower oil. International Journal of Precision Engineering and Manufacturing—Green Technology, 2020, 7(2): 337–345
45. Haq M A U, Hussain S, Ali M A, Farooq M U, Mufti N A, Pruncu C I, Wasim A. Evaluating the effects of nano-fluids based MQL milling of IN718 associated to sustainable productions. Journal of Cleaner Production, 2021, 310: 127463
46. Li H N, Wang J P, Wu C Q, Zhao Y J, Xu, J, Liu X L, Zhu W Q. Damage behaviors of unidirectional CFRP in orthogonal cutting: a comparison between single- and multiple-pass strategies. Composites Part B: Engineering, 2020, 185: 107774

47. Ni C B, Zhu L D. Investigation on machining characteristics of TC4 alloy by simultaneous application of ultrasonic vibration assisted milling (UVAM) and economical-environmental MQL technology. Journal of Materials Processing Technology, 2020, 278: 116518
48. Jang D Y, Jung J, Seok J. Modeling and parameter optimization for cutting energy reduction in MQL milling process. International Journal of Precision Engineering and Manufacturing—Green Technology, 2016, 3(1): 5–12
49. Zhang Y B, Li C H, Jia D Z, Li B K, Wang Y G, Yang M, Hou Y L, Zhang X W. Experimental study on the effect of nanoparticle concentration on the lubricating property of nanofluids for MQL grinding of Ni-based alloy. Journal of Materials Processing Technology, 2016, 232: 100–115
50. Said Z, Arora S, Farooq S, Sundar L S, Li C H, Allouhi A. Recent advances on improved optical, thermal, and radiative characteristics of plasmonic nanofluids: academic insights and perspectives. Solar Energy Materials and Solar Cells, 2022, 236: 111504
51. Said Z, Jamei M, Sundar L S, Pandey A K, Allouhi A, Li C H. Thermophysical properties of water, water and ethylene glycol mixture-based nanodiamond + Fe_3O_4 hybrid nanofluids: an experimental assessment and application of data-driven approaches. Journal of Molecular Liquids, 2022, 347: 117944
52. Gaurav G, Sharma A, Dangayach G S, Meena M L. Assessment of jojoba as a pure and nano-fluid base oil in minimum quantity lubrication (MQL) hard-turning of Ti–6Al–4V: a step towards sustainable machining. Journal of Cleaner Production, 2020, 272: 122553
53. Yang M, Li C H, Said Z, Zhang Y B, Li R Z, Debnath S, Ali H M, Gao T, Long Y Z. Semiempirical heat flux model of hard-brittle bone material in ductile microgrinding. Journal of Manufacturing Processes, 2021, 71: 501–514
54. Qu S S, Gong Y D, Yang Y Y, Wang W W, Liang C Y, Han B. An investigation of carbon nanofluid minimum quantity lubrication for grinding unidirectional carbon fibre-reinforced ceramic matrix composites. Journal of Cleaner Production, 2020, 249: 119353
55. Gao T, Li C H, Yang M, Zhang Y B, Jia D Z, Ding W F, Debnath S, Yu T B, Said Z, Wang J. Mechanics analysis and predictive force models for the single-diamond grain grinding of carbon fiber reinforced polymers using CNT nano-lubricant. Journal of Materials Processing Technology, 2021, 290: 116976
56. Gao T, Li C H, Zhang Y B, Yang M, Jia D Z, Jin T, Hou Y L, Li R Z. Dispersing mechanism and tribological performance of vegetable oil-based CNT nanofluids with different surfactants. Tribology International, 2018, 131: 51–63
57. Wojciechowski S, Matuszak M, Powałka B, Madajewski M, Maruda R W, Królczyk G M. Prediction of cutting forces during micro end milling considering chip thickness accumulation. International Journal of Machine Tools and Manufacture, 2019, 147: 103466
58. Kline W A, DeVor R E, Lindberg J R. The prediction of cutting forces in end milling with application to cornering cuts. International Journal of Machine Tool Design and Research, 1982, 22(1): 7–22
59. Martellotti M E. An analysis of the milling process. Transaction of ASME, 1941, 63: 677–695
60. Duan Z J, Yin Q A, Li C H, Dong L, Bai X F, Zhang Y B, Yang M, Jia D Z, Li R Z, Liu Z Q. Milling force and surface morphology of 45 steel under different Al_2O_3 nanofluid concentrations. The International Journal of Advanced Manufacturing Technology, 2020, 107(3): 1277–1296
61. Zhao Y J, Xu W H, Xi C Z, Liang D T, Li H N. Automatic and accurate measurement of microhardness profile based on image processing. IEEE Transactions on Instrumentation and Measurement, 2021, 70: 1–9
62. Yang M, Li C H, Zhang Y B, Jia D Z, Zhang X P, Hou Y L, Li R Z, Wang J. Maximum undeformed equivalent chip thickness for ductile-brittle transition of zirconia ceramics under different lubrication conditions. International Journal of Machine Tools and Manufacture, 2017, 122: 55–65
63. Huang B T, Zhang Y B, Wang X M, Chen Y, Cao H J, Liu B, Niu X L, Li C H. Experimental evaluation of wear mechanism and grinding performance of SG wheel in machining nickel-based alloy GH4169. Surface Technology, 2021, 50(12): 62–70 (in Chinese)
64. Said Z, Ghodbane M, Boumeddane B, Tiwari A K, Sundar S, Li C H, Aslfattahi N, Bellos E. Energy, exergy, economic and environmental (4E) analysis of a parabolic trough solar collector using MXene based silicone oil nanofluids. Solar Energy Materials and Solar Cells, 2022, 239: 111633
65. Duan Z J, Li C H, Zhang Y B, Dong L, Bai X F, Yang M, Jia D Z, Li R Z, Cao H J, Xu X F. Milling surface roughness for 7050 aluminum alloy cavity influenced by nozzle position of nanofluid minimum quantity lubrication. Chinese Journal of Aeronautics, 2021, 34(6): 33–53
66. Zhang Y R, Guo K, Sun J. Investigation on the milling performance of amputating clamping supports for machining with industrial robot. The International Journal of Advanced Manufacturing Technology, 2019, 102: 3573–3586
67. Shi Y B, Li H L, Li J C, Zhi D J, Zhang X Y, Liu H, Wang H Q, Li H Y. Development, optimization and evaluation of emodin loaded nanoemulsion prepared by ultrasonic emulsification. Journal of Drug Delivery Science and Technology, 2015, 27: 46–55
68. Jia D Z, Zhang N Q, Liu B, Zhou Z M, Wang X P, Zhang Y B, Mao C, Li C H. Particle size distribution characteristics of electrostatic minimum quantity lubrication and grinding surface quality evaluation. Diamond & Abrasives Engineering, 2021, 41(3): 89–95 (in Chinese)
69. Liu M Z, Li C H, Zhang Y B, An Q L, Yang M, Gao T, Mao C, Liu B, Cao H J, Xu X F, Said Z, Debnath S J, Jamil M, Ali H M, Sharma S. Cryogenic minimum quantity lubrication machining: from mechanism to application. Frontiers of Mechanical Engineering, 2021, 16(4): 649–697
70. Jia D Z, Li C H, Zhang Y B, Yang M, Cao H J, Liu B, Zhou Z M. Evaluation of electro traction grinding performance and surface morphology of titanium alloy biological lubricant. Chinese Journal of Mechanical Engineering, 2022, 58(5): 198–211 (in Chinese)
71. Liu M Z, Li C H, Cao H J, Zhang S, Chen Y, Liu B, Zhang N Q, Zhou Z M. Research progresses and applications of CMQL machining technology. China Mechanical Engineering, 2022, 33(5): 529–550 (in Chinese)
72. Shi Z, Guo S M, Liu H J, Li C H, Zhang Y B, Yang M, Chen Y,

Liu B, Zhou Z M, Niu X L. Experimental evaluation of minimum quantity lubrication of biological lubricant on grinding properties of GH4169 nickel-base alloy. Surface Technology, 2021, 50(12): 71–84 (in Chinese)

73. Wang X M, Li C H, Zhang Y B, Yang M, Zhou Z M, Chen Y, Liu B, Wang D Z. Research progress on enabled atomization and supply system of minimum quantity lubrication. Surface Technology, 2022, 51(9): 1–14 (in Chinese)